Journal of Materials Chemistry C

ROYAL SOCIETY OF CHEMISTRY

PAPER

View Article Online
View Journal | View Issue

Cite this: J. Mater. Chem. C, 2025, 13, 22253

Tunable photoluminescence, visible-light excitation, and high quantum yield in scalable copper cluster halide emitters for optoelectronics

Ulises Eli Cercas,[a] Diego Solis-Ibarra,[b] Fernando Cortés-Guzman,[c] Iván Enrique Martínez-Merlin,[a] Vojtech Jancik,[de] Juan Carlos Alonso-Huitrón,[b] Disnel Ferrera-Carracedo,[b] Ciro Falcony-Guajardo,[f] María de Jesús Rosales-Hoz[g] and Jesús Uriel Balderas-Aguilar *[b]

Received 27th June 2025,
Accepted 30th September 2025

DOI: 10.1039/d5tc02475g

rsc.li/materials-c

Zero-dimensional copper halide phosphors have emerged as efficient, less toxic alternatives to lead-based systems. Here, we report a bromide–iodide alloyed cluster, $TPA_2[Cu_4Br_2I_4]$, stabilized by optoelectronically inert tetrapropylammonium (TPA^+), featuring strong Cu–Cu interactions, visible-light excitation (λ_{ex} = 444 nm), green-yellow emission (λ_{em} = 512 nm), and a high photoluminescence quantum yield (~95%). Temperature- and power-dependent photoluminescence studies reveal a dual emission mechanism arising from excitonic recombination in *cis* and *trans* isomers. Time-dependent DFT calculations elucidate the photoinduced electronic redistribution and structural relaxation underlying this behavior. The material is readily synthesized *via* mechanochemistry and processed into thin films by spin coating or aerosol-assisted chemical vapor deposition (AACVD). Its integration into polymer composites demonstrates its practical utility for lighting applications. Finally, the successful extension of the alloying strategy to other cations such as $MTPP^+$ highlights its versatility for designing tunable copper cluster halide phosphors aimed at next-generation optoelectronic and lighting technologies.

1. Introduction

The discovery of lead halide perovskite quantum dots has spurred a revolution in metal halide phosphors, where efficient emission is often governed by exciton confinement within nanocrystals.[1] However, the photoluminescence in these systems is highly sensitive to particle size and surface defects, making long-term emission stability and reproducibility challenging. In contrast, zero-dimensional (0D) metal halide systems achieve high photoluminescence quantum yields (PLQYs) without relying on quantum confinement. Their discrete metal halide units suppress exciton migration, enabling strong and stable emission through stoichiometric and structural control rather than size-dependent effects.[2]

To mitigate the toxicity of lead, copper(I) halides have emerged as promising alternatives. Their luminescence is strongly influenced by coordination geometry (tetrahedral, trigonal planar, or linear), distortions, and Cu···Cu interactions. Most reported Cu(I) halides exhibit self-trapped exciton (STE)-driven emission, achieving high PLQY but requiring high-energy excitation (>3.5 eV), which exceeds the operating range of cost-effective blue-light LEDs and lasers commonly used in modern devices.[3,4]

Recently, 0D luminescent copper cluster halides containing $[Cu_4I_6]^{2-}$ subunits, stabilized by bulky organic cations, have demonstrated visible-light excitation.[5–8] Metallophilic interactions within Cu_4 clusters, arising from Cu···Cu distances shorter than their van der Waals radii, reduce the HOMO–LUMO gap, enabling excitation in the visible range. Furthermore, organic spacers – unlike inorganic cations – offer tunability in optical properties and luminescence through band alignment and weak interactions, making PLQY highly

[a] Tecnológico Nacional de México, Instituto Tecnológico de Tlalnepantla, DEPI, Av. Instituto Tecnológico S/N, Col. La Comunidad, Tlalnepantla de Baz 54070, Mexico
[b] Instituto de Investigaciones en Materiales, Universidad Nacional Autónoma de México, Ciudad Universitaria, A.P. 70-360, Coyoacán, Mexico City, Mexico. E-mail: jubalderas@iim.unam.mx
[c] Facultad de Química, Universidad Nacional Autónoma de México, Ciudad Universitaria, CDMX 04510, Mexico
[d] Instituto de Química, Universidad Nacional Autónoma de México, Ciudad Universitaria, Ciudad de México 04510, Mexico
[e] Centro Conjunto de Investigación en Química Sustentable UAEM-UNAM, Carretera Toluca-Atlacomulco km. 14.5, Toluca, Estado de México 50200, Mexico
[f] Centro de Investigación y de Estudios Avanzados del IPN (CINVESTAV), Departamento de Física, Av. Instituto Politécnico Nacional 2508, San Pedro Zacatenco, Gustavo A. Madero, CDMX, Mexico
[g] Centro de Investigación y de Estudios Avanzados del IPN (CINVESTAV), Departamento de Química, Av. Instituto Politécnico Nacional 2508, San Pedro Zacatenco, Gustavo A. Madero, CDMX, Mexico

dependent on spacer selection. For example, highly conjugated methyltriphenylphosphonium spacers facilitate metal-to-ligand charge transfer (MLCT) and halide-to-ligand charge transfer (XLCT) mechanisms that contribute to luminescence, but at the cost of reduced PLQY.[9] In contrast, non-conjugated tetraalkylammonium cations have been used to stabilize $[Cu_4Br_6]^{2-}$ clusters, yielding ultrabroad red-peaking luminescence with near-unity PLQY; however, in this system the excitation peaks at $\lambda < 400$ nm,[10,11] significantly limiting its activation under visible-light sources. During the preparation of this manuscript, an independent study reported $TPA_2[Cu_4Br_2I_4]$ as a down-converting and UV-protective layer in perovskite solar cells.[12] Initially poor film morphology obtained from antisolvent-assisted spin-coating (DMF solutions) was greatly improved by vacuum-assisted dry spin-coating and post-annealing. Optimized devices retained 90% and 80% of their initial power conversion efficiencies after UV exposures of 66.07 and 210.7 kWh m^{-2}, respectively, with a slight drop in efficiency (23.09% to 22.24%) due to reduced short-circuit current density. This highlights the broad utility and potential of the mixed-halide approach.

Here, we significantly advance the understanding and practical utilization of bromide–iodide alloyed copper-cluster halides. Single crystals synthesized from an optimized CuI : TPA-Br (4 : 2) precursor ratio yield $[Cu_4Br_2I_4]^{2-}$ luminescent clusters with an exceptionally broad excitation band centered at 444 nm and bright green-yellow emission at 513 nm, accompanied by a remarkably high photoluminescence quantum yield (~95%). Structural analysis *via* single-crystal X-ray diffraction, complemented by electronic structure calculations, provides detailed insight into the excited-state dynamics responsible for the broadband emission. In addition to outstanding optical properties, the phosphor demonstrates excellent processability—enabling high-quality films *via* spin coating and aerosol-assisted chemical vapor deposition (AACVD) from acetonitrile solutions—and rapid, scalable synthesis through gram-scale mechanochemistry. Extending this strategy by replacing TPA^+ with methyltriphenylphosphonium ($MTPP^+$) spacers further confirms the structural and luminescent tunability, underscoring the wide-ranging applicability of this approach. Collectively, these results establish the $A_2[Cu_4Br_2I_4]$ halide-alloying strategy as a versatile and promising synthetic pathway for developing advanced phosphors suitable for next-generation optoelectronic and lighting technologies.

2. Methodology

2.1 Materials and reagents

Copper(I) iodide (CuI, 98%), copper(I) bromide (CuBr, 98%), tetrapropylammonium iodide (TPA-I), tetrapropylammonium bromide (TPA-Br), hypophosphorous acid (H_3PO_2, 50% weight in water), acetonitrile (ACN, ≥99.8%), and dimethylformamide (DMF, ≥99.9%) were purchased from Sigma-Aldrich and used without further purification.

2.2 Synthesis of $TPA_2[Cu_4Br_2I_4]$ and related single crystals

Single crystals with varying Br/I ratios ($TPA_2[Cu_4Br_{6-x}I_x]$, x = 0–6) were synthesized by dissolving the appropriate molar ratios of CuBr, CuI, and TPA halides in a mixture of acetonitrile (3 mL) and hypophosphorous acid (H_3PO_2, 100 μL). The solutions were sonicated in an ultrasonic bath for 10 minutes to form clear, homogenous solutions, which were left to evaporate at room temperature over 24 hours, yielding millimeter-sized single crystals.

The reagent quantities for each composition are summarized in Table 1.

2.3 Synthesis of powder phosphors

Phosphor powders were synthesized in multigram-scale quantities by manually grinding CuI (24 mmol, 4.571 g) with TPA-Br (12 mmol, 3.195 g) or MTPP-Br (12 mmol, 4.287 g) in an agate mortar, using H_3PO_2 (1 mL) as a reactive medium. After 5 minutes of grinding, a green paste-like powder exhibiting bright luminescence under 405 nm excitation was obtained (see Video S1, SI). The resulting phosphors were thoroughly rinsed with ethyl acetate and dried overnight at 40 °C, yielding 7.35 g (96%) for the TPA^+-based material and 8.13 g (92%) for the $MTPP^+$ analogue.

2.4 Synthesis of spin-coated films

CuI (2.4 mmol, 0.4571 g) and TPA-Br (1.2 mmol, 0.3195 g) were dissolved in a mixture of ACN (3 mL) and H_3PO_2 (100 μL) using an ultrasonic bath for 10 minutes to form a homogeneous yellowish solution. The solution was spin-coated onto previously cleaned glass substrates (25 × 25 × 1 mm) at 3500 rpm for 60 seconds.

2.5 Synthesis of AACVD films

Thin films were deposited using aerosol-assisted chemical vapor deposition (AACVD). A precursor solution was prepared by dissolving CuI (2.4 mmol, 0.4571 g) and TPA-Br (1.2 mmol, 0.3195 g) in a mixture of ACN (30 mL) and H_3PO_2 (1 mL) under magnetic stirring for 10 minutes. The solution was split between two ultrasonic nebulizers operating at 1.7 MHz, and the generated mists were transported to hot glass substrates (70 °C) using N_2 gas (3 L min^{-1}) as the carrier. The deposition process lasted 3 minutes. The AACVD setup and methodology followed a previously reported design.[13]

Table 1 Reagent composition for $TPA_2[Cu_4Br_{6-x}I_x]$ single-crystals

	CuBr	CuI	TPA-Br	TPA-I
x	mmol (g)	mmol (g)	mmol (g)	mmol (g)
0	2.4 (0.3443)	0	1.2 (0.3195)	0
1	1.8 (0.2582)	0.6 (0.1143)	1.2 (0.3195)	0
2	1.2 (0.1721)	1.2 (0.2285)	1.2 (0.3195)	0
3	0.6 (0.0861)	1.8 (0.3428)	1.2 (0.3195)	0
4	0	2.4 (0.4571)	1.2 (0.3195)	0
5	0	2.4 (0.4571)	0.6 (0.1598)	0.6 (0.1889)
6	0	2.4 (0.4571)	0	1.2 (0.3759)

2.6 Structural characterization

Single-crystal X-ray diffraction (SCXRD): single crystals were analyzed on a Bruker Smart Apex Duo diffractometer equipped with an Apex II CCD detector and Incoatec IμS microsource (Mo-Kα radiation λ = 0.71073 Å) at 100 K. Data were collected using ω scans, integrated with SAINT,[14] and corrected for absorption using SADABS.[15] Structures were solved by direct methods with SHELXT,[16] and refined using full-matrix least-squares on F^2 with SHELXL-2019/3[17] within the ShelXle GUI.[18] All non-hydrogen atoms were refined anisotropically. Hydrogen atoms were placed in idealized positions. The asymmetric unit contains half of the $[Cu_4X_6]^{2-}$ anion and parts of three crystallographically independent Pr_4N^+ cations (half, quarter, and quarter). The cation that appears whole has an occupancy of 0.5 for all atoms as it is located on a 4_2 screw axis and was allowed to relax from the special position using PART-1. The nitrogen atoms of the other two cations are located on the inversion center of the $\bar{4}$ rotoinversion axes. The anion is located on an inversion center and the *n* glide plane, and therefore is completely disordered. Additionally, the three crystallographically independent X positions all feature disorder between Br and I atoms, where the proportion was refined for each position separately using free variables resulting in a precise formula $TPA_2[Cu_4Br_{2.16}I_{3.84}]$ for the analyzed crystal. The Cu–X bond lengths are left unrestrained even though they are slightly shorter than the average values reported in the literature, because they represent the statistical average of all the positions, they can have in the anion due to the disorder, and even bonds to two neighboring copper atoms need not be equal. This led to a best fit to the experimental electron density. The hydrogen atoms of the C–H bonds were placed in idealized positions, and refined with U_{iso} tied to the parent atom. The disordered copper, halogen atoms, and tetrapropylammonium cation were refined with U_{ij} restraints (SIMU, RIGU, EADP) implemented in SHELXL-2019/3. Powder X-ray diffraction (PXRD): patterns were recorded on an Ultima IV Rigaku diffractometer using Cu-Kα radiation (λ = 1.5418 Å) over a 2θ range of 5°–55° with a step size of 0.02°.

2.7 Optical and photophysical characterization

UV-Vis spectroscopy: absorption spectra were measured using a PerkinElmer Lambda 25 UV-vis spectrophotometer over the 300–1100 nm wavelength range.

Photoluminescence (PL): excitation and emission spectra were recorded on an Edinburgh Instruments FS5 fluorometer equipped with a 150 W ozone-free xenon arc lamp and Czerny–Turner monochromators. Temperature-dependent photoluminescence and decay times were recorded using a cryostat and a 375 ± 5 nm picosecond pulsed diode laser, while photoluminescence quantum yield (PLQY) was measured at room temperature using an integrating sphere on the same fluorimeter. The measurements of the spectral power distribution (SPD) in the wavelength range λ = 400–800 nm of the LED lamp and the converting phosphor layer studied were performed with a CCD spectroradiometer LISUN LMS-9000B with an integrating sphere. Thermogravimetric analysis (TGA) was performed on a TGA Q5000 IR system (TA Instruments, New Castle, DE, USA) under nitrogen flow. Approximately 5 mg of dry sample was heated from 30 °C to 400 °C at a rate of 5 °C min^{-1}.

2.8 Computational methodology

Density functional theory (DFT) and time-dependent DFT (TD-DFT) calculations were performed using the Gaussian 16 software package.[19] We used *t*HCTHhyb as the functional,[20] and Jorge-TZP, triple zeta valence quality plus polarization function, was used as the basis set.[21] Previous to the calculation, the ground state was optimized for the two possible configurations of $[Cu_4Br_2I_4]^{2-}$, one isomer with the bromine atoms opposite, marked as *trans*, and the isomer with adjacent positions of the iodide atoms as *cis*. The organic molecules were not included within the computational analysis.

3. Results and discussion

3.1 Synthesis and crystallographic structure

$TPA_2[Cu_4Br_2I_4]$ single crystals were synthesized using a room-temperature solvent evaporation method, employing a low boiling point solvent and H_3PO_2 as a reducing agent to prevent Cu(I) oxidation (see Experimental section for details). The resulting green-colored cuboid single crystals, shown in Fig. 1a and b under ambient and 405 nm illumination, respectively, highlight the material's distinct luminescence properties.

Single-crystal X-ray diffraction (SCXRD) analysis was performed to determine the atomic structure of $TPA_2[Cu_4Br_2I_4]$, revealing that it is isostructural to $TPA_2[Cu_4Br_6]$. The phosphor crystallizes in the tetragonal crystal system (space group $P4_2/n$), with lattice parameters $a = b$ = 15.773 Å and c = 16.055 Å. Its structure comprises four slightly distorted trigonal planar $[CuX_3]^{2-}$ subunits, connected by shared edges to form a $[Cu_4X_6]^{2-}$ cluster (X = Br, I). The asymmetric unit contains half of the $[Cu_4X_6]^{2-}$ anion and parts of three crystallographically independent TPA^+ cations (half, quarter, and quarter), as depicted in Fig. 1c (see Tables S1 and S2 for more crystallographic details).

Within the Cu_4 tetrahedron, the Cu–Cu distances are shorter than the sum of the van der Waals radii of Cu(I) (2.80 Å), indicating strong metallophilic interactions.[8,22] Furthermore, four iodine and two bromine atoms are disordered across six positions around the cluster. Consequently, two distinct halide configurations are expected depending on bromine positioning: *cis*, where bromine atoms are adjacent, and *trans*, where they are alternately positioned (Fig. 1d). The structural integrity of these disordered clusters is preserved by the bulky TPA^+ organic spacers. To assess the geometric stability of the cluster, the effective ionic radii of the TPA^+ molecules and $[Cu_4Br_2I_4]^{2-}$ clusters were calculated to be 2.545 and 5.314 Å, respectively. Their radius ratio is approximately 0.479, which falls within Pauling's octahedral stability window (0.41–0.73),[23] supporting the robustness of the crystal structure.

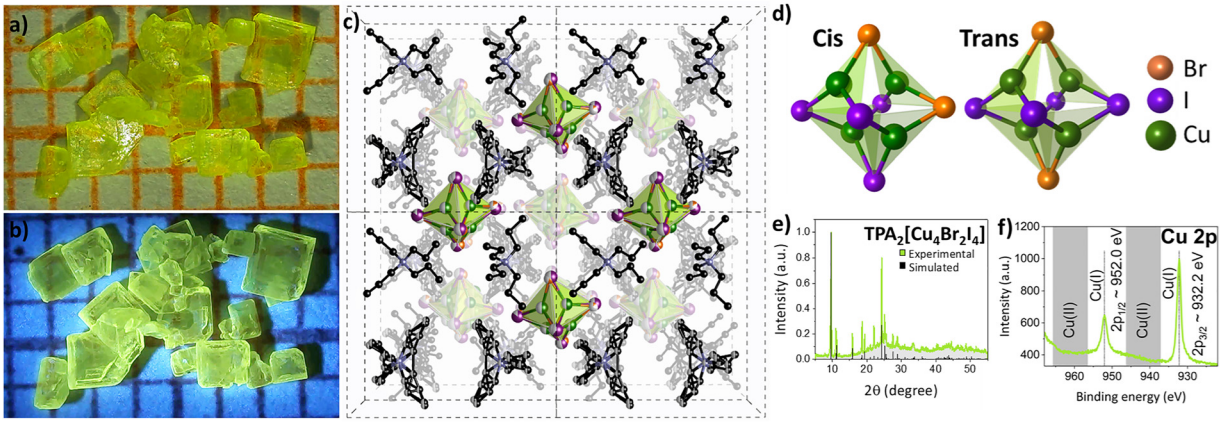

Fig. 1 Digital photographs of $TPA_2[Cu_4Br_2I_4]$ single crystals under (a) ambient lighting and (b) 405 nm illumination, highlighting their strong luminescence. (c) Crystal structure of $TPA_2[Cu_4Br_2I_4]$, determined by single-crystal X-ray diffraction. (d) Illustration of two possible halide arrangements (''*cis*'' and ''*trans*'') within the $[Cu_4Br_2I_4]^{2-}$ clusters, dependent on the positions occupied by bromine ions. (e) Experimental powder X-ray diffraction pattern from ground single crystals, showing excellent agreement with the simulated pattern. (f) High-resolution Cu 2p core-level XPS spectrum, confirming the exclusive presence of Cu(I) species.

The phase purity of the obtained solids was corroborated by powder X-ray diffraction (PXRD), which shows an excellent agreement between the experimental PXRD patterns and the pattern calculated from the single crystal structure (Fig. 1e). On the other hand, X-ray photoelectron spectroscopy (XPS) confirms the presence of Cu, Br, and I in the sample (Fig. S1a–c). The high-resolution Cu 2p core level spectrum shown in Fig. 1f displays two binding energy peaks at 952.0 (Cu $2p_{1/2}$) and 932.2 eV ($2p_{3/2}$), consistent with Cu(I) species. Notably, the absence of the Cu(II) related satellite peaks confirms that Cu remains in the +1 oxidation state, which is crucial for the material's stability and optimal luminescence performance.

3.2 Optical and photoluminescence measurements

3.2.1 Optical absorption and photoluminescence quantum yield. Fig. 2a presents the UV-vis absorption, photoluminescence (PL) emission and excitation spectra of the single crystals recorded at 300 K. The absorption spectrum spans the

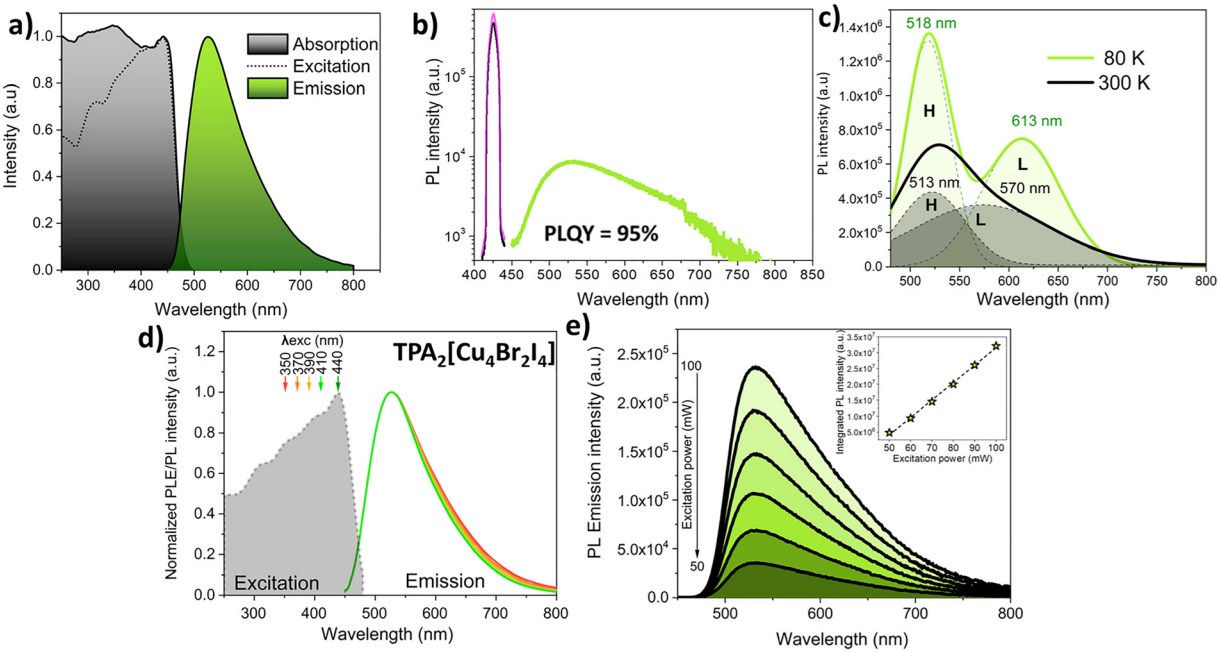

Fig. 2 (a) UV-Vis absorption, photoluminescence (PL) excitation, and PL emission spectra of $TPA_2[Cu_4Br_2I_4]$ single crystals at room temperature. (b) PL quantum yield (PLQY) measured using an integrating sphere, highlighting an exceptionally high efficiency (~95%). (c) Temperature-dependent PL emission spectra (80 and 300 K), showing clearly resolved high-energy (H) and low-energy (L) emission bands obtained by Gaussian deconvolution. (d) Normalized PL emission spectra under varying excitation wavelengths, confirming emission from the same excited state. (e) Power-dependent PL intensity plot demonstrating linearity, indicative of intrinsic excitonic emission rather than defect-mediated recombination.

UV-visible light range, with a prominent absorption peak at 440 nm. An optical band gap of ~2.8 eV, determined from Tauc plot calculations, indicates strong visible-light absorption (Fig. S2a). The excitation spectrum spans the UV-visible region, peaking at 444 nm, in good agreement with the absorption spectrum.

The presence of excitonic absorption peaks at room temperature suggests a high exciton binding energy, likely supported by the non-conjugated TPA^+ spacers that provide a low-polarizability environment.[24] This strong exciton confinement is reflected in the photoluminescence behavior, where the emission spectrum exhibits a broad asymmetric band peaking at 526 nm. Additionally, PLQY measurements reveal an impressive 95% efficiency (Fig. 2b), confirming minimal self-absorption despite the low Stokes shift (69 nm). These properties indicate a highly efficient luminescent process, warranting a deeper exploration of the underlying emission mechanism.

3.2.2 Temperature-dependent PL: exciton–phonon interactions. To get deeper insight into the luminescence mechanism, the temperature-dependent PL spectra (80–300 K) were recorded and deconvoluted by Gaussian fitting. Fig. 2c compares the emission spectra obtained at 300 and 80 K, where both spectra resolve into two distinct bands: a high-energy band (H) and a low-energy band (L). The position, intensity and full width at half maximum (FWHM) exhibit notable temperature dependence.

To systematically analyze this behavior, PL spectra were collected at 20 K increments and deconvoluted into H and L bands. The normalized temperature-dependent bands are independently plotted in Fig. S2b and c. At 80 K, both bands appear narrowed and seem to be decoupled. Upon heating from 80 to 300 K, the H-band shifts slightly from 518 to 513 nm, with its FWHM increasing from 53 to 66 nm. The L-band undergoes a more pronounced shift, from 613 to 570 nm, with a corresponding FWHM increase from 93 to 110 nm. This blue shift and broadening are characteristic of increased electron–phonon coupling, commonly observed in metal halide luminescent materials.[25] At low temperatures, structural rigidity minimizes distortions in the excited state, effectively decoupling excitons from phonons.

In addition, the ratio of integrated H and L bands (H/L) changes from 0.65 at 300 K to 0.99 at 80 K, suggesting that at room temperature, energy transfer between the two states is efficient, while at 80 K, the energy barrier becomes too large to overcome.

Complementary photoluminescence measurements under *in situ* heating (320–380 K, Fig. S2f) revealed a gradual emission decrease. This process was fully reversible upon cooling, indicating thermally activated quenching rather than permanent structural degradation, consistent with enhanced exciton–phonon interactions at elevated temperatures. Thermogravimetric analysis (Fig. S2g) confirmed high thermal stability, with no significant mass loss up to 105 °C. A minor 2% loss occurred between 105 and 200 °C, followed by linear mass reductions of ~10% at 255 °C and ~38% at 320 °C, closely matching the expected mass contribution of tetrapropylammonium bromide in the sample.

3.2.3 PL lifetimes and excited-state relaxation. To better understand the interplay between the two emission bands, PL lifetimes were recorded at 300 and 80 K using a 375 nm laser while monitoring the emission at 513 and 518 nm, respectively (Fig. S2d–f).

At 80 K, the emission mechanisms decouple, as evidenced by distinct double exponential decay times of 4.07 and 11.39 μs. In contrast, at 300 K, the decay profiles become indistinguishable, yielding a monoexponential decay of 3.59 μs. These results, together with the H/L ratio changes, confirm that the energy barriers between excited states are low, enabling excitons to efficiently cross between states and achieve thermal equilibrium. At 300 K, this results in uniform green emission from $TPA_2[Cu_4Br_2I_4]$, facilitated by the effective coupling of multiple excited states.

3.2.4 Composition-dependent luminescence: the role of Br/I alloying. Both H and L emission bands originate from the same excited state, as evidenced by their identical emission profiles under various excitation wavelengths (Fig. 2d). However, using only bromide or iodide precursor salts fails to produce the green-emitting material, underscoring the critical role of Br/I mixtures. To explore this further, single crystals with varying Br/I ratios ($TPA_2[Cu_4Br_{6-x}I_x]$, x = 0–6) were synthesized. The normalized excitation and emission spectra (Fig. S3a–f) reveal distinct luminescence behaviors:

- (x = 0) formation of UV-excitable red-emitting $TPA_2[Cu_4Br_6]$, exhibiting excitation-independent emission from a single excited state.
- (x = 1–3) excitation-dependent emission, indicating the coexistence of $[Cu_4Br_6]^{2-}$ and $[Cu_4Br_2I_4]^{2-}$ clusters rather than a single $[Cu_4Br_5I]^{2-}$ species. As iodine content increases, the contribution of $[Cu_4Br_2I_4]^{2-}$ dominates.
- (x = 5) the emergence of a new white-emitting species when excited at 330 nm, alongside $TPA_2[Cu_4Br_2I_4]$.
- (x = 6) emission shifts to pure white, corresponding to the formation of the UV-excitable $TPA_2[Cu_2I_4]$, with non-emissive impurities.

The XRD patterns of ground single crystals (Fig. S4) support this evolution, revealing gradual lattice expansion as Br is replaced by I. For $x > 4$, diffraction peaks characteristic of the zero-dimensional $TPA_2[Cu_2I_4]$ phase become prominent. These results are consistent whit previous reports and emphasize the necessity of precise Br/I balance to achieve the unique luminescent properties of this phosphor.[12]

3.2.5 Power-dependent PL: ruling out defect-driven emission. To determine whether the emission arises from excitons localized at permanent defects in the crystal lattice, power-dependent luminescence spectra were recorded. If emission were defect-driven, increasing excitation power would gradually populate defect states, eventually leading to intensity saturation.[26] However, Fig. 2e reveals a linear increase in PL intensity with rising excitation power density, with no signs of saturation or spectral changes. This strongly suggests that the emission originates from intrinsic electronic states rather than

defect-mediated recombination, reinforcing the material's high photoluminescence stability and suitability for optoelectronic applications.

3.3 Electronic structure analysis

The presence of two distinct emission bands has been consistently reported in a variety of $A_2[Cu_4X_6]$ (X = Cl, Br, I) phosphors. A widely accepted explanation attributes the low-energy emission band to copper-centered d → s, p transitions accompanied by halide-to-metal charge transfer (^{3}XMCT), while the high-energy emission band is typically associated with ligand-centered excited states, involving metal-to-ligand (^{3}MLCT) and halide-to-ligand (^{3}XLCT) charge transfer processes. However, this mechanism inherently requires the A^+ cationic species to exhibit electron-accepting characteristics, as demonstrated in systems employing methyltriphenyl-phosphonium ($MTPP^+$),[5] $[(p\text{-phenylenediamine})_4(H_2PO_2)_6]^+$,[27] or (benzo-15-crown-5)$_2$-NaH_2O^+,[28] where π-conjugation facilitates charge transfer interactions.

In stark contrast, TPA^+ lacks any π-conjugated system, rendering it optoelectronically inert and incapable of participating in MLCT or HLCT processes. Consequently, the conventional MLCT/HLCT-based explanation for the two emission bands cannot account for the photophysical behavior observed in $TPA_2[Cu_4Br_2I_4]$.

TD-DFT has been extensively employed to investigate copper-based systems, consistently achieving strong agreement with experimental data by accurately describing charge-transfer phenomena and excited-state geometric distortions.[19,29–32] Specifically, the *t*HCTHhyb functional has proven effective in reproducing key excited-state properties, including absorption and emission energies, as well as the accurate depiction of triplet states.[33] Building on this foundation, we conducted an electronic structure analysis of the $[Cu_4Br_2I_4]^{2-}$ clusters in both *cis* and *trans* configurations, using the optimized *t*HCTHhyb functional. This analysis, leveraging single-crystal structural data (Fig. 3), enabled a detailed investigation of the ground and excited states, providing critical insights into the origins of the high (H) and low (L) energy emission bands.

Notably, the *cis* and *trans* structures are virtually isoenergetic in the ground state (ΔE = 0.1 kcal mol^{-1}), consistent with the observed disorder in the SCXRD analysis. The excited-state dynamics are represented using configurational coordinate diagrams (Fig. 3a and b). Vertical photoinduced $S_0 \rightarrow S_1$ transitions for the *trans* and *cis* structures occur at 3.12 eV and 3.09 eV, respectively—values slightly higher than the experimental band-gap (2.8 eV), but within reasonable theoretical deviation.

From the S_1 state, both structures engage in a highly efficient intersystem crossing (ISC) cascade into the ^{3}CC triplet states, initiating from T_6 and T_7, for the *cis* and *trans* configurations, respectively (see Fig. S5). These triplet states sequentially relax internally to the T_1 state, which subsequently deactivates radiatively to S_0. This multi-step relaxation pathway, characteristic of triplet-state dynamics, directly accounts for the long photoluminescence (PL) decay times observed experimentally. For the *trans* configuration, the energy gap between T_1 and a high-energy S_0 conformer is 2.36 eV, followed by a final relaxation of 0.31 eV to the ground-state minimum. In contrast, the *cis* configuration exhibits a smaller T_1 to S_0 energy gap of 1.79 eV, accompanied by a more pronounced structural rearrangement of 0.63 eV upon reaching the ground state.

The calculated emission energies from these relaxed T_1 states align well with the experimentally observed H and L emission bands, measured at 2.4 eV and 2.02 eV, respectively.

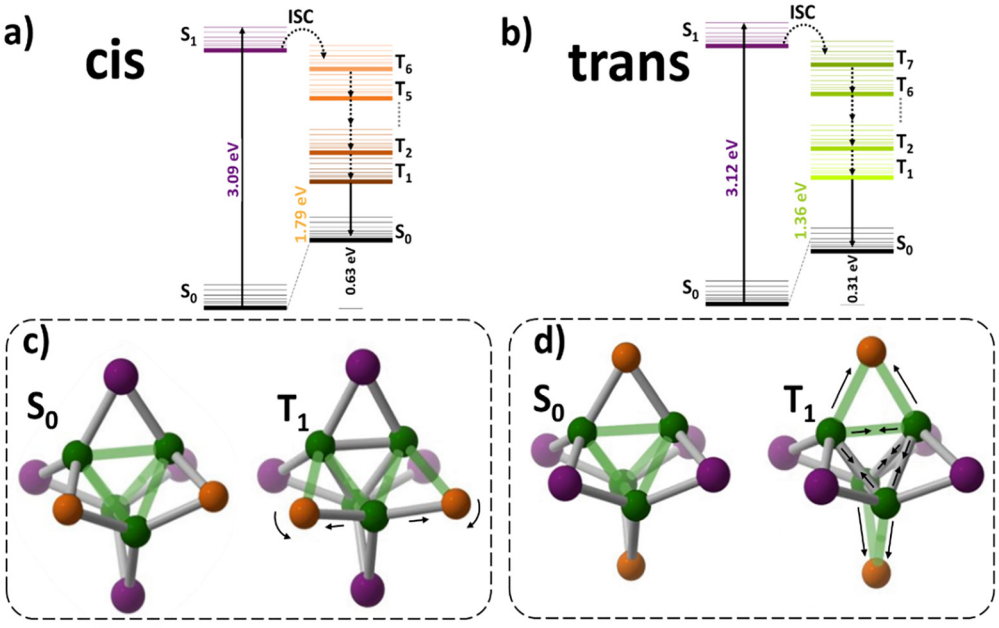

Fig. 3 Simplified energy scheme of the electronic levels for the $[Cu_4Br_2I_4]^{2-}$ in (a) *cis* and (b) *trans* configurations. Structural changes from S_0 to T_1 for the (c) *cis* and (d) *trans* configurations are also shown. Covalent interactions are depicted in gray, while weak interactions are highlighted in green.

Moreover, the calculated exciton energies—defined by the energy difference between the optimized S_0 and T_1 states—are 525.36 nm for the *trans* structure and 692.65 nm for the *cis* structure. This theoretical behavior is consistent with the experimental trend observed as temperature increases, where the two emission bands undergo a progressive blue shift.

The strong agreement between theory and experiment validates our model, allowing for a confident interpretation of the photoinduced electronic redistribution and the associated structural changes governing the dual emission behavior.

In our previous work,[34] we established a mechanism where photoexcitation induces electron density redistribution within the valence shell of copper atoms, triggering subsequent geometric rearrangements. This mechanism is directly applicable to the $[Cu_4Br_2I_4]^{2-}$ isomers, where the structural changes observed can be attributed to photoinduced electron transfer between atoms within the cluster. Specifically, in the *trans* configuration, a redistribution of 0.16 e is observed, where two copper atoms and four iodide atoms donate electron density to the remaining two copper atoms and two bromide atoms. In the *cis* configuration, three copper and three iodine atoms transfer 0.28 e to the rest of the cluster.

These photoinduced electron redistributions result in distinct structural distortions during the excited-state relaxation process, which in turn directly influence the dual emission behavior. The connection between these theoretical predictions and the experimentally observed high (H) and low (L) energy emission bands is further reinforced by the calculated exciton energies and structural dynamics.

As illustrated in Fig. 3c and d, the structural changes that occur between the S_0 and T_1 states differ significantly between the two isomers. For the *cis* configuration (Fig. 3c), the most prominent geometric change is an expansion of the Br–Cu–Br angle from 119.05° to 131.3°, coupled with a bromide ion shifting 0.5 Å away from the cluster. This angular distortion, which stabilizes the T_1 state, makes the *cis* configuration more susceptible to electron–phonon coupling, directly contributing to the pronounced temperature dependence of the L emission band energy.

Conversely, in the *trans* configuration (Fig. 3d), the primary structural change is an increase in the Br···Br distance by 0.29 Å and a reduction in Cu···Cu distances, with the most significant contraction of 0.31 Å between the copper atoms that lose electron density. This structural reorganization is

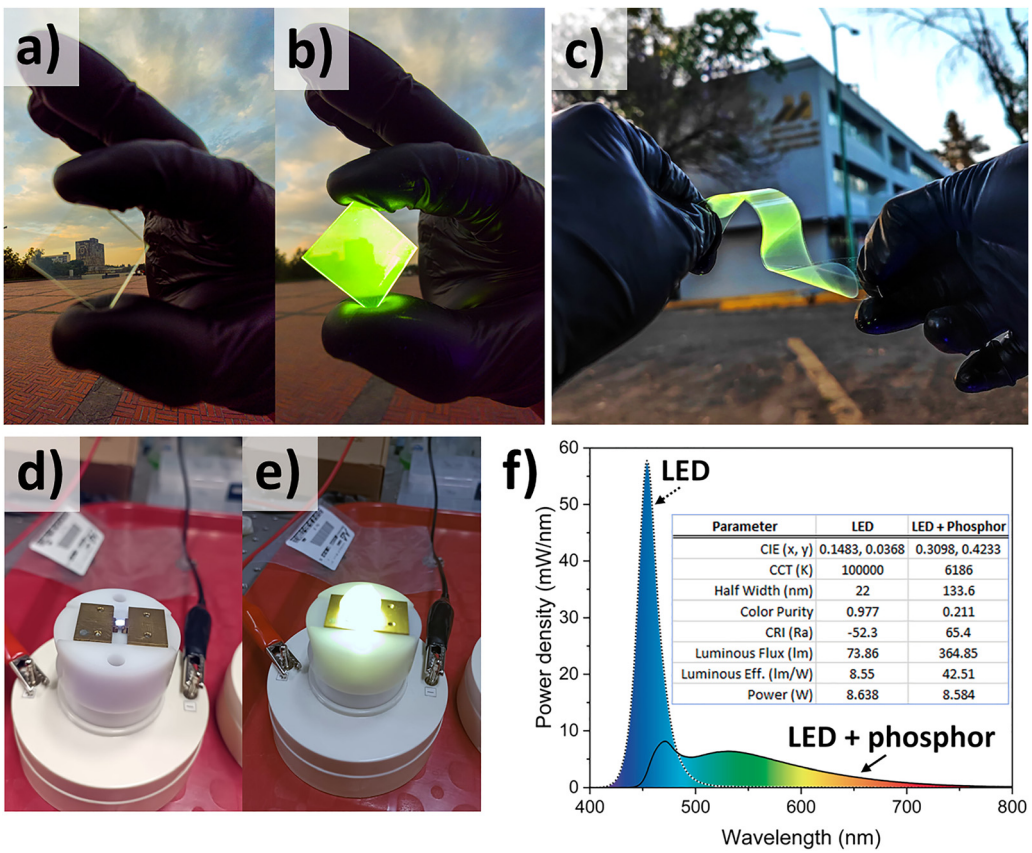

Fig. 4 (a) Digital photograph of spin-coated $TPA_2[Cu_4Br_4I_2]$ film under ambient illumination, and (b) 405 nm illumination, illustrating homogeneous coverage and minimal scattering. (c) Digital photograph of the phosphor film deposited by AACVD onto a flexible PET substrate under simultaneous ambient and 405 nm illumination, highlighting flexibility and luminescence retention. (d) Photograph of a bare 440 nm LED and (e) the same LED coated with the phosphor–polymer composite, evidencing efficient wavelength conversion to a warm-white emission. (f) Electroluminescence spectra comparing the bare 10 W 440 nm LED (dotted line) and the converted LED with the phosphor/EVA composite (continuous line). The inset table summarizes key performance differences between both configurations.

consistent with the energy stabilization of the T_1 state, leading to the observed H emission band.

The strong correlation between our theoretical analysis and the experimental observations—including the temperature-dependent redshift of the two emission bands and the long-lived triplet state dynamics—provides compelling support for the proposed model. These findings establish a clear connection between photoinduced structural reorganization and dual emission behavior, not only deepening our understanding of this system but also offering a robust framework for designing copper-based luminescent materials with tunable properties.

3.4 Processability and potential application

The high processability and scalability of the phosphor were demonstrated through rapid grams-scale mechanochemical synthesis. This straightforward approach, achieved by manually grinding precursor salts with H_3PO_2 in an agate mortar, yields the targeted material in less than 10 minutes, confirmed by powder XRD matching simulated patterns (Fig. S6). Such remarkable simplicity and speed underline the clear potential for industrial-scale production.

Versatile deposition methods underscore the practical applicability of this phosphor. Films prepared *via* spin coating on top of glass substrate (Fig. 4a and b), and aerosol-assisted chemical vapor deposition (AACVD) on a flexible PET sheet (Fig. 4c), successfully retain the luminescent properties. SEM analysis (Fig. S7a and b) confirms good substrate coverage, revealing distinct morphological signatures: spin-coated films exhibit rod-shaped grains ($\sim 0.3 \times 1$ μm) coalescing in island-like formations (characteristic of centrifugal-driven crystallization); whereas AACVD-produced films feature well-packed, faceted grains (5–8 μm) resembling the tetragonal crystalline morphotype. AACVD, in particular, stands out for its versatility, scalability, and adaptability to diverse device architectures including non-conventional flexible substrates.

To illustrate practical potential, composite films incorporating mechanochemically synthesized phosphor within a polymer matrix were successfully employed as wavelength-converting phosphors atop a commercial high-power royal-blue LED (10 W), efficiently generating warm-white emission (Fig. 4d and e). Spectral details are provided in Table S3, emphasizing the material's suitability for practical optoelectronic applications.

To highlight the simplicity, versatility, and broad applicability of our halide alloying strategy, we substituted the TPA^+ spacer with methyltriphenylphosphonium ($MTPP^+$). This phosphor was synthesized *via* the rapid mechanochemical route, similarly achieving tunable and highly promising luminescent properties. Photoluminescence excitation and emission spectra of the resulting $MTPP_2[Cu_4Br_2I_4]$ phosphor (Fig. 5a) show excitation-independent emission, with no spectral shifts observed upon varying the excitation wavelength, analogous to the TPA-based system. Compared to the TPA analogue, the MTPP emission maximum is slightly red-shifted (545 nm, Fig. S8a) and requires a more complex spectral deconvolution, suggesting multiple contributing processes that may include MLCT/HLCT in addition to *cis*/*trans* configuration-related emission (Fig. S8b). For comparison, spectra of the previously reported iodide-only $MTPP_2[Cu_4I_6]$ system are included, further highlighting the effectiveness of halide alloying in precisely modulating emission characteristics. The PLQY of the alloyed system was measured to be 72%, comparable to the $MTPP_2[Cu_4I_6]$ composition.[8]

Powder XRD analysis of $MTPP_2[Cu_4Br_2I_4]$ reveals excellent structural agreement with simulated patterns from $MTPP_2[Cu_4I_6]$, exhibiting diffraction peak shifts due to lattice contraction upon bromide substitution (Fig. 5b). These results underscore the generality and power of this alloying approach, enabling targeted control over luminescence properties across diverse organic spacers employed in luminescent $[Cu_4X_6]^{2-}$ clusters.

Collectively, these findings illustrate the exceptional versatility and technological promise of $A_2[Cu_4Br_{6-x}I_x]$ phosphors. This approach could be extended to other UV-excitable

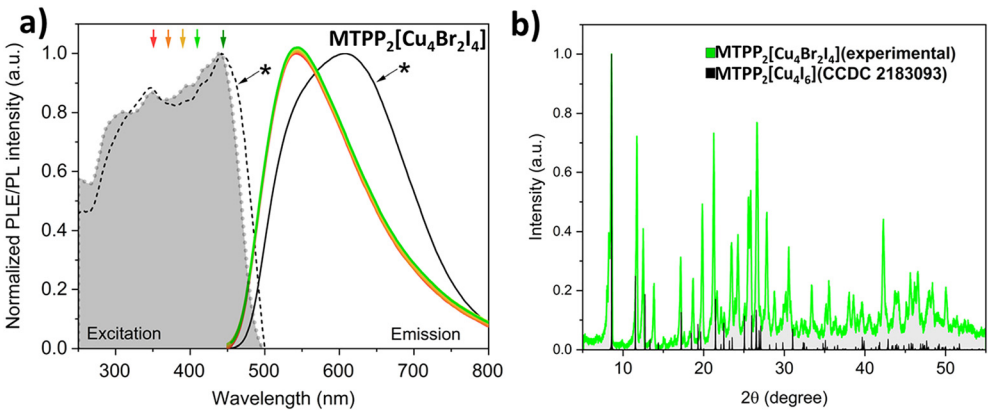

Fig. 5 (a) Normalized PL emission spectra of mechanochemically synthesized $MTPP_2[Cu_4Br_2I_4]$ recorded under different excitation wavelengths, confirming emission from a single luminescent center. For comparison, PL excitation (dashed line, marked *) and emission (solid line, marked *) spectra of the previously reported $MTPP_2[Cu_4I_6]$, synthesized by the same method, are included as reference. (b) Powder XRD pattern of $MTPP_2[Cu_4Br_2I_4]$ alongside the simulated XRD pattern of $MTPP_2[Cu_4I_6]$, clearly demonstrating peak shifts consistent with lattice contraction due to bromide substitution.

$A_2[Cu_4Br_6]$ structures reported with A-cations such as ethyltriphenylphosphonium ($ETPP^+$),[35] tetrabutylphosphonium (TBP^+),[36] and tetraethylphosphonium (TEP^+).[26] Furthermore, it may provide a strategy to activate systems that are otherwise non-emissive at room temperature, such as the $FA_2[Cu_4Br_6]$ phase,[37] where longer A-site-Cu^+ distances structurally favor non-radiative decay. In such cases, halide alloying could modify the cluster environment, stabilize excited states, and promote radiative recombination. The demonstrated simplicity, scalability, and versatility in processing, open exciting practical pathways for commercial applications, such as large-scale lighting systems and flexible optoelectronic devices. Current ongoing investigations, including optimized growth of large centimeter-scale single crystals, advanced polymer composite development, refinement of spin-coating techniques for low-scattering solar concentrators, and versatile AACVD film deposition onto unconventional substrates (textured, flexible, elastic), promise significant extensions of the practical applicability of these phosphors, paving the way toward next-generation luminescent and optoelectronic technologies.

4. Conclusions

In summary, the bromide–iodide alloying approach introduced here yields a high-performance copper-cluster halide phosphor ($TPA_2[Cu_4Br_2I_4]$) with outstanding photoluminescence efficiency (~95% PLQY) and desirable visible-light excitation characteristics. Detailed photophysical analyses from experimental data demonstrate intrinsic exciton recombination pathways, unaffected by defect-mediated losses, and temperature-dependent studies offer deeper insights into exciton–phonon interactions underpinning the luminescence mechanism. The detailed electronic structure analysis revealed that the dual emission behavior (H and L bands) arises from distinct structural dynamics in the *cis* and *trans* isomers, driven by photo-induced electron density redistribution and geometric reorganization. The calculated exciton energies and their temperature-dependent redshift are in strong agreement with experimental observations, providing a robust framework for understanding the emission mechanism in this system.

The phosphor's processability was validated through rapid mechanochemical synthesis scalable to industrial production, alongside successful thin-film fabrication *via* spin coating and AACVD on conventional and flexible substrates. Demonstrated integration into polymer composites and subsequent warm-white LED application further underscores practical relevance. Importantly, this alloying strategy proves transferable to diverse organic spacers, significantly broadening its applicability across various luminescent platforms.

Author contributions

Ulises Eli Cercas: investigation (lead), formal analysis, writing – original draft preparation. Diego Solis-Ibarra: resources, validation, writing – review & editing. Iván Enrique Martínez-Merlin: investigation, validation, resources, funding acquisition (supporting). Fernando Cortés-Guzmán: formal analysis, writing – original draft preparation. Vojtech Jancik: formal analysis, validation, writing – original draft preparation. Disnel Ferrera-Carracedo: investigation (supporting). Juan Carlos Alonso-Huitrón, Ciro Falcony-Guajardo, María de Jesús Rosales-Hoz: resources, methodology, validation. Jesús Uriel Balderas-Aguilar: conceptualization, project administration, funding acquisition (lead), data curation, visualization, validation, writing – original draft preparation (lead).

Conflicts of interest

There are no conflicts to declare.

Data availability

CCDC 2456019 ($TPA_2[Cu_4Br_2I_4]$) contains the supplementary crystallographic data for this paper.[38]

The authors confirm that the data supporting the findings of this study are available within the article and its supplementary information (SI). Supplementary information: characterization data of new compounds. See DOI: **https://doi.org/10.1039/d5tc02475g**.

Acknowledgements

The authors gratefully acknowledge the valuable technical support of V. Guerrero-Sosa, A. Tejeda-Cuz, M. García-Hipólito, C. Ramos-Vilchis, A. Pompa-García, L. Huerta-Arcos, and K. Reyes-Morales from IIM-UNAM. We also thank the staff of LUME (RRID:SCR_024400), particularly O. Novelo-Peralta and L. Bazán-Díaz, for assistance with SEM characterization, and A. Ronquillo-Arvizu from ICML-UNAM for his technical support. Additional assistance was provided by M. Guerrero-Cruz and Z. Rivera-Álvarez from the Physics Department, and M. Leyva-Ramírez from the Chemistry Department of CINVESTAV-IPN. The first and seventh authors acknowledge SECIHTI for the award of a master's and doctoral fellowship, respectively. This work was primarily supported by DGAPA-UNAM under the PAPIIT-UNAM project IA104025, with additional financial support provided by Tecnológico Nacional de México through project number 14636.

References

1 J. T. Griffiths, F. Wisnivesky Rocca Rivarola, N. J. L. K. Davis, R. Ahumada-Lazo, J. A. Alanis, P. Parkinson, D. J. Binks, W. Y. Fu, F. De La Pena, M. B. Price, A. Howkins, I. Boyd, C. J. Humphreys, N. C. Greenham and C. Ducati, *ACS Appl. Energy Mater.*, 2019, **2**, 6998–7004.
2 J. Almutlaq, J. Yin, O. F. Mohammed and O. M. Bakr, *J. Phys. Chem. Lett.*, 2018, **9**, 4131–4138.
3 Z. Ma, X. Ji, S. Lin, X. Chen, D. Wu, X. Li, Y. Zhang, C. Shan, Z. Shi and X. Fang, John Wiley and Sons Inc, 2023, preprint, DOI: **10.1002/adma.202300731**.

4 I. D. Strelnik, I. E. Kolesnikov, A. A. Kalinichev, T. P. Gerasimova, K. D. Akhmadgaleev, I. R. Dayanova and A. A. Karasik, Elsevier Ltd, 2024, preprint, DOI: 10.1016/j.mencom.2024.06.001.
5 L. Xie, Z. Liu, H. Yang, K. Chen, N. Lv, H. Pi, X. Chen, X. Li, Z. Liu, S. Li, Z. Wang, Y. Wang and B. Chen, *Adv. Opt. Mater.*, 2024, **12**(27), 2401050.
6 R. An, Q. Wang, Y. Liang, P. Du, P. Lei, H. Sun, X. Wang, J. Feng, S. Song and H. Zhang, *Angew. Chem., Int. Ed.*, 2025, **64**(1), e202413991.
7 J. Huang, B. Su, E. Song, M. S. Molokeev and Z. Xia, *Chem. Mater.*, 2021, **33**, 4382–4389.
8 P. Fu, S. Geng, R. Mi, R. Wu, G. Zheng, B. Su, Z. Xia, G. Niu, J. Tang and Z. Xiao, *Energy Environ. Mater.*, 2024, **7**(1), e12518.
9 Y. Guo, Y. F. Fu, J. Wu, J. L. Qi, Y. M. Zhang, Q. F. Huang, W. Liu and S. P. Guo, *Inorg. Chem. Front.*, 2025, **12**, 1909–1917.
10 S. Chen, J. Gao, J. Chang, Y. Li, C. Huangfu, H. Meng, Y. Wang, G. Xia and L. Feng, *ACS Appl. Mater. Interfaces*, 2019, **11**, 17513–17520.
11 D. Y. Li, Q. Tan, M. P. Ren, W. Q. Wang, B. L. Zhang, G. Niu, Z. Gong and X. W. Lei, *Sci. China Mater.*, 2023, **66**, 4764–4772.
12 Z. Liu, Z. Liu, L. Deng, S. Guo, Y. Wang, L. Xie, N. Lv, H. Yang, L. Xujie, B. Chen and Y. Zhan, *Small*, 2025, **21**(11), 2500630.
13 J. U. Balderas-Aguilar, C. Falcony-Guajardo, G. A. Velázquez-Nevárez, V. González-Pérez, E. Martínez-Guerra and F. S. Aguirre-Tostado, *Adv. Mater. Technol.*, 2022, **7**(5), 2100657.
14 Bruker AXS Inc. Madison, 2007, preprint.
15 L. Krause, R. Herbst-Irmer, G. M. Sheldrick and D. Stalke, *J. Appl. Crystallogr.*, 2015, **48**, 3–10.
16 G. M. Sheldrick, *Acta Crystallogr., Sect. A:Found. Adv.*, 2015, **71**, 3–8.
17 G. M. Sheldrick, *Acta Crystallogr., Sect. C:Struct. Chem.*, 2015, **71**, 3–8.
18 C. B. Hübschle, G. M. Sheldrick and B. Dittrich, *J. Appl. Crystallogr.*, 2011, **44**, 1281–1284.
19 M. Iwamura, S. Takeuchi and T. Tahara, *J. Am. Chem. Soc.*, 2007, **129**, 5248–5256.
20 C. Adamo and V. Barone, *J. Chem. Phys.*, 1999, **110**, 6158–6170.
21 L. S. C. Martins, F. E. Jorge and S. F. Machado, *Mol. Phys.*, 2015, **113**, 3578–3586.
22 D. A. Popy and B. Saparov, Royal Society of Chemistry, 2024, preprint, DOI: 10.1039/d4tc04153d.
23 T. J. Jacobsson, M. Pazoki, A. Hagfeldt and T. Edvinsson, *J. Phys. Chem. C*, 2015, **119**, 25673–25683.
24 J. I. Climente, J. L. Movilla and J. Planelles, *J. Phys. Chem. Lett.*, 2024, **15**, 7379–7386.
25 D. Ju, M. Zhou, P. Ran, H. Li, Y. M. Yang and T. Jiang, *ACS Mater. Lett.*, 2023, **5**, 2978–2986.
26 D. A. Popy, Y. Singh, Y. Tratsiak, A. M. Cardoza, J. M. Lane, L. Stand, M. Zhuravleva, N. Rai and B. Saparov, *Aggregate*, 2024, **5**(5), e602.
27 S. Zhou, Y. Chen, K. Li, X. Liu, T. Zhang, W. Shen, M. Li, L. Zhou and R. He, *Chem. Sci.*, 2023, **14**, 5415–5424.
28 S. A. Khan, N. Z. Khan, J. Ahmed, M. Runowski, S. M. Alshehri, S. Agathopoulos, S. J. Teat and J. Li, *J. Mater. Chem. C*, 2025, **13**(8), 4055–4068.
29 G. Capano, U. Rothlisberger, I. Tavernelli and T. J. Penfold, *J. Phys. Chem. A*, 2015, **119**, 7026–7037.
30 G. Capano, T. J. Penfold, M. Chergui and I. Tavernelli, *Phys. Chem. Chem. Phys.*, 2017, **19**, 19590–19600.
31 S. Xu, J. Wang, F. Zhao, H. Xia and Y. Wang, *J. Mol. Model.*, 2015, **21**, 1–10.
32 A. Agena, S. Iuchi and M. Higashi, *Chem. Phys. Lett.*, 2017, **679**, 60–65.
33 A. C. Tsipis, Royal Society of Chemistry, 2014, preprint, DOI: 10.1039/c4ra04921g.
34 L. Gutiérrez-Arzaluz, D. I. Ramírez-Palma, L. G. Ramírez-Palma, J. E. Barquera-Lozada, J. Peon and F. Cortés-Guzmán, *Chem. – Eur. J.*, 2019, **25**, 775–784.
35 D. Y. Li, J. H. Wu, X. Y. Wang, X. Y. Zhang, C. Y. Yue and X. W. Lei, *Chem. Mater.*, 2023, **35**, 6598–6611.
36 X. Yang, X. Yang, Z. Liu, Q. Qian, S. M. H. Qaid, A. S. Aldwayyan, B. Wang and S. Zhao, *Adv. Opt. Mater.*, 2025, **13**(12), 2403177.
37 D. E. Belikova, S. A. Fateev, V. N. Khrustalev, E. I. Marchenko, E. A. Goodilin, S. Wang and A. B. Tarasov, *Dalton Trans.*, 2023, **52**, 7152–7160.
38 CCDC 2456019: Experimental Crystal Structure Determination, 2025, DOI: 10.5517/ccdc.csd.cc2nfpf7.

